

Comparative study on the effect of iron and silicon addition on the microstructure and mechanical properties of aluminium–lithium powder atomized alloys

F. H. SAMUEL

Département des Sciences appliquées, Université du Québec à Chicoutimi, 555, Boulevard de l'Université, Chicoutimi, Québec, Canada G7H 2B1

G. CHAMPIER, P. TODESCHINI, J. H. TORRES

Laboratoire de Physique du Solide, Ecole des Mines, Nancy 54042, France

The present work was conducted on a wide series of Al–Si, Al–Li, Al–Li–Si and Al–Li–Fe alloys produced by centrifugal atomization. Solidification in Al–Si powders occurs by heterogeneous nucleation at the interface with the atmosphere, followed by propagation of the solidification front towards the particle centre. Addition of 3% Li to the Al–Si alloys shifts the ternary eutectic point to less than 4% Si. The eutectic structure is a mixture of aluminium and AlLiSi phases. For Al–2.5% Li–1.3% Fe, in addition to δ' -Al₃Li phase precipitates, Al₃Fe (needle-like) and Al₆Fe (globular) phase precipitates are present. The volume fraction of Al₃Fe dispersoids is not affected by the presence of the grain boundaries, and is enough to strengthen the precipitation-free zones.

1. Introduction

In 1982, Aziz [1] established the dependence of the partition coefficient, k , on the solid–liquid interface velocity. A rapid variation in k value occurs when the interface velocity reaches its critical value $V = D_L/\lambda$, where D_L is the diffusion coefficient of solute in liquid and λ is the interatomic distance. When the cooling rate exceeds 10^4 °C s⁻¹, the critical velocity is approximately 20 m s⁻¹. Therefore, trapping of solute in solid is believed to be the physical phenomenon responsible for the planar stability of the solid–liquid interface.

It was also noted that the chemical potential of the solute increased during the course of solidification. It led to slowness of the transport phenomenon and hence trapping/segregation of solute in solidified material. Nevertheless, this process did not take place until the enthalpy of the solid was inferior to that of the liquid. This condition is achievable when the temperature is lower than T_0 in Fig. 1 (from Murray [2]) for hypoeutectic Al–Si alloys. It is evident from the T_0 curve that an undercooling of about 100 K or more is likely to occur in the Al–12% Si alloy at the beginning of solidification. In this case, stabilization of a planar interface by surface tension is easy if k is close to unity. For $k = 0.8$, the critical velocity, V , is only 2 m s⁻¹.

The addition of Li to Al–Si alloys leads to the precipitation of AlLiSi compound [3]. When the silicon atomic concentration is lower than that of lithium, all the silicon is included in the AlLiSi precipitates; the lithium remains in solid solution and, if the lithium concentration is large enough, δ' -Al₃Li

phase precipitation takes place, too. An improvement in the mechanical properties and in the density can thus be expected.

An effective way of improving the strength and ductility of binary Al–Li alloys is to introduce incoherent dispersoid particles and to refine the grain size using the rapid solidification technique. During the annealing of Al–Li binary alloys, soft continuous precipitate-free zones form along the grain boundaries and, hence, early cracks. The importance of the dispersoid particles is to change the mechanism of deformation from heterogeneous into more homogeneous which, in turn, improves the alloy ductility [4].

From the Al–Fe binary diagram [5], four intermetallic phases are expected, depending on the Fe concentration. These are as follows:

Al ₆ Fe	orthorhombic, metastable
Al ₉ Fe ₂	monoclinic, metastable
Al ₃ Fe	monoclinic, stable
Al ₅ Fe ₂	monoclinic or orthorhombic, metastable

In the present alloy, Al–2.5 wt % Li–1.3 wt % Fe, Al₃Fe appears to be the essential phase. It should also be noted that the solubility of Fe in molten Li is very low, 0.014 at % at 930 °C. However, the ternary Al–Li–Fe phase diagram is not yet known.

The present study deals briefly with the following aspects:

- (a) centrifugal pulverization,
- (b) degassing,

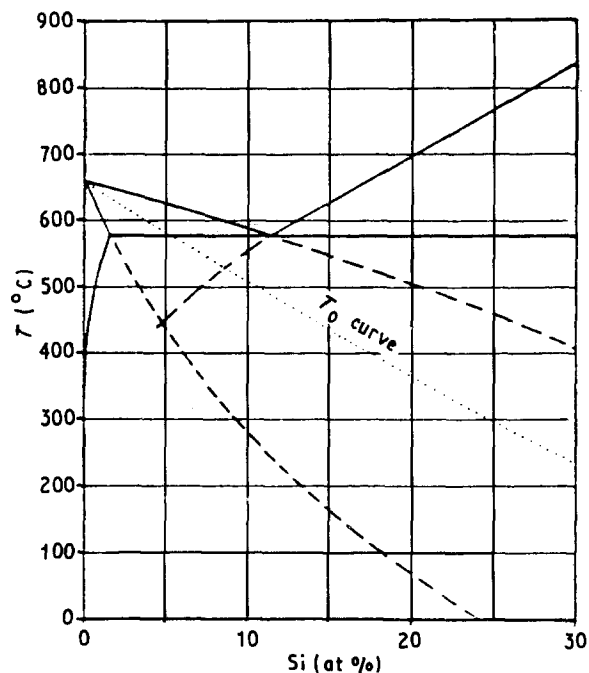


Figure 1 T_0 curve and extension of solidus and liquidus for Al-Si system [2].

- (c) hot extrusion,
- (d) heat treatment (solution treatment, quenching, ageing),
- (e) alloy characterization at each step,
- (f) evaluation of mechanical properties, and
- (g) determining the mechanism that controls the plastic deformation.

The technique of powder atomization by centrifugal pulverization has been developed by Pratt and Whitney Aircraft-United Technologies Corporation, USA. Publications concerning this technique are mostly proprietaries and patents [6-8].

2. Experimental procedure

Alloys used in the present study were prepared from high-purity metals ($\sim 99.9\%$) under an inert atmosphere of argon. Rapidly solidified powders were produced by the conventional centrifugal atomizing process, with helium used as the cooling medium. Ingots of 400 g were melted in a graphite crucible having an orifice of 1 mm diameter and coated with a thick layer of boron nitride refractory. The atomizing chamber was evacuated and filled with helium up to 1 bar. The liquid metal was ejected on to a rotating atomizer with a helium overpressure. The chemical composition and designation of the alloys are given in Table I.

The microstructure of powder particles (with sizes ranging between 25 and 50 μm) was examined by light microscopy, scanning electron microscopy (SEM, operating at 15 kV), and transmission electron microscopy (TEM, operating at 200 kV). The precipitates were identified by X-ray diffraction using a $\text{CoK}\alpha$ source.

Tensile tests were carried out with an Instron-type tensile machine. The gauge length of the specimens was 18 mm and the diameter was 4 mm. The strain rate was $7.5 \times 10^{-4} \text{ s}^{-1}$.

TABLE I Alloy specifications

Designation	Composition (wt %)				Initial pour temperature ($^{\circ}\text{C}$)
	Si	Li	Sr	Fe	
AS	13.2	—	—	—	715
ASR	12.3	—	0.7	—	715
ALS1	1	2.5	—	—	730
ALS2	2	2.5	—	—	730
ALS4	4	2.5	—	—	730
ALS8	8	2.5	—	—	730
AL3	—	2.5	—	—	750
AL3F2	—	2.5	—	1.3	800

3. Results and discussion

3.1. Microstructure characterization

3.1.1. Al-Si alloys

The X-ray diffraction of Al-Si and Al-Si-Sr powders revealed only α and Si phases (Fig. 2). A significant increase in the intensity of the $(011)_{\alpha}$ peak was observed with a remarkable decrease in the intensity of the $(111)_{\alpha}$ peak after hot extrusion. As these diffractions were produced from specimens where the surface exposed to the X-rays was parallel to the extrusion direction, it is reasonable to conclude that the deformation texture is of $\langle 111 \rangle$ type [9].

Optical microstructures of polished sections prepared from as-melt-quenched loose powders are shown in Fig. 3. Two main observations could be made:

(i) Fine microstructure consisting of α -Al crystals possessing the form of dendrites or cells. As the diameter of the powder particles decreases, the secondary dendrite arms tend to disappear and be entirely replaced by a cellular structure.

(ii) Coarse microstructure of equiaxed dendrites of α -Al.

From these micrographs and others, some thermal parameters could be calculated and are listed in Table II. These calculations are based on the assumption that there is only one nucleation event and the ratio of the external surface, S^* , to the solid-liquid interface surface, S , is unity.

The variation in the microstructural details, even in the interior of the same powder particle, is explicable in terms of

- (a) the existence of two solidification mechanisms, first adiabatic (high interface velocity and recalescence), then isothermal (progress of the interface controlled by the external flux), or
- (b) the variation in the S^*/S ratio.

The calculations made by Levi and Mehrabian [10, 11] show that the first explanation is correct.

Thin foils were prepared from loose powders with diameters in the range 25-50 μm . It was found that intercellular or interdendritic materials contained Si particles that were either in the form of elongated needles (7 μm long and 0.2 μm thick) or else spherical (with diameters in the range 0.15 to 0.35 μm). For Al-Si-Sr powders, the Si particles were always spherical, with diameters ranging between 50 and 100 nm (Fig. 4).

TABLE II Thermal parameters calculated from the microstructure of powder particles with different sizes

Parameter	Particle size, d (μm)					
	25	50	80	100	175	200
h ($10^4 \text{W m}^{-2} \text{K}^{-1}$)	2.4	1.5	1.0	0.9	0.8	0.6
L_{min} (10^{-3}m s^{-1})	12.4	7.7	5.2	4.6	4.1	3.1
\dot{T} (10^5K s^{-1})	11.0	3.4	1.4	1.0	0.72	0.34
Calculated SDAS* (μm)	0.46	0.67	0.90	1.0	1.10	1.5
Measured SDAS (μm)	0.5–0.9	0.6–1.0	0.8–1.1	0.8–1.5	1.0–1.7	1.1–1.7

*SDAS: Secondary dendrite arm spacing.

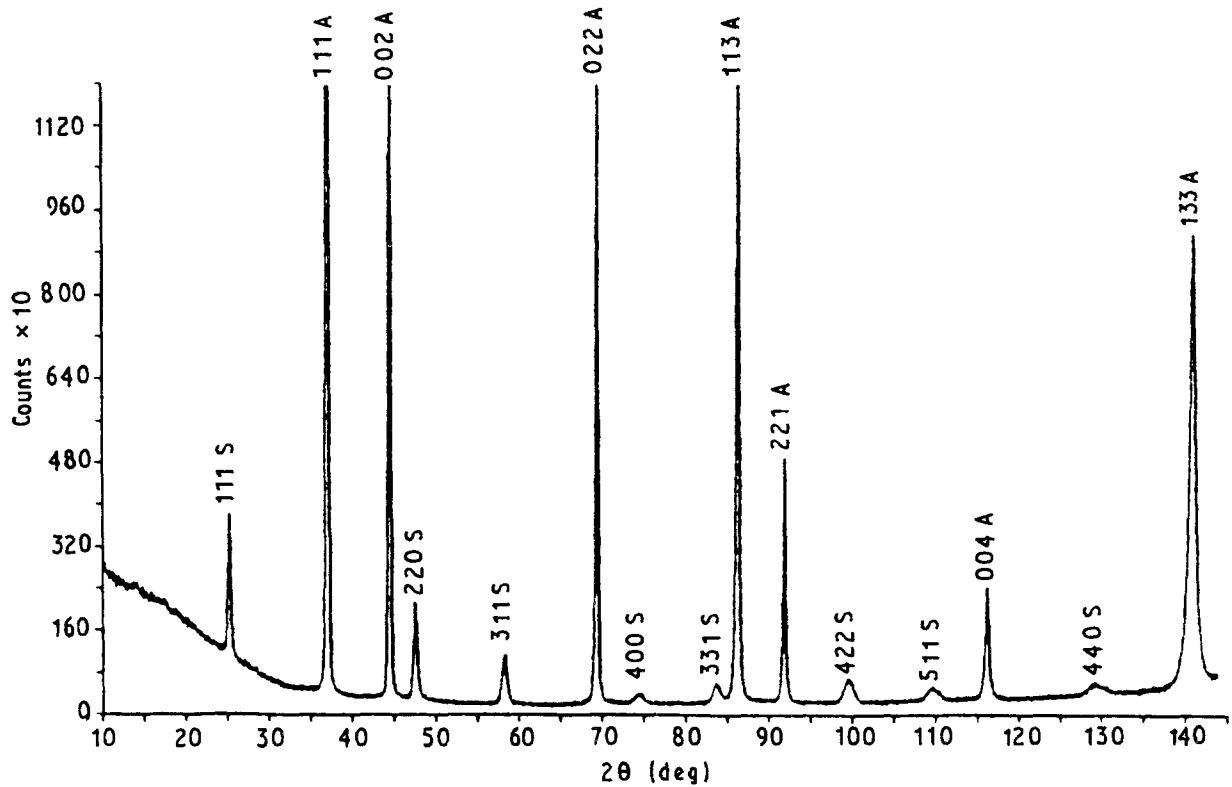


Figure 2 X-ray diffraction patterns obtained from Al-12% Si melt-quench powders.

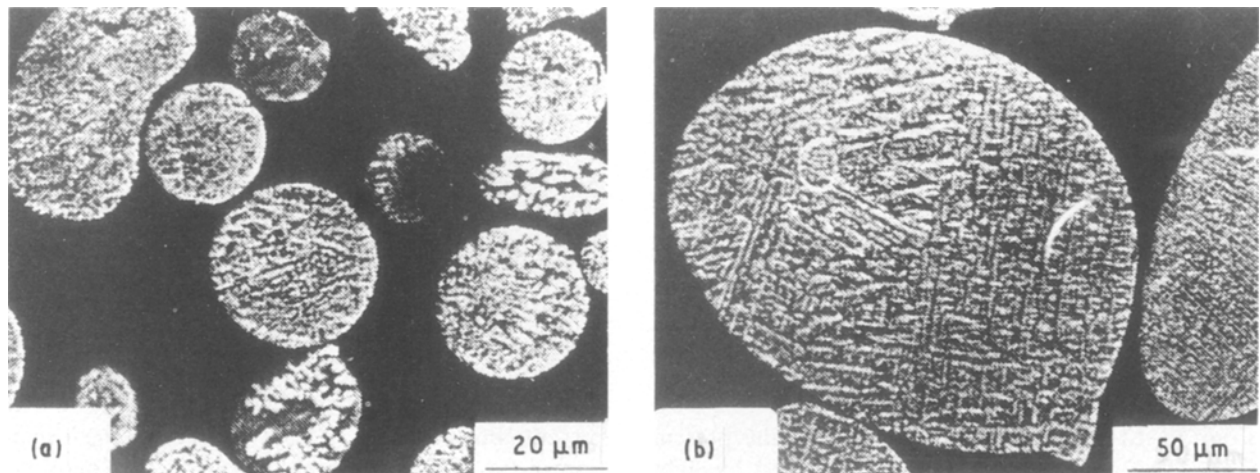


Figure 3 Optical microstructure of loose powders of Al-12% Si alloy with two different particle sizes.

TEM examination of extruded powders allows for more precise measurements of α -grain and Si particle size (Fig. 5). About 400 silicon particles over surfaces of $5.8 \times 10^{-11} \mu\text{m}^2$ were measured. Taking the thick-

ness of the thin foil to be about $0.7 \mu\text{m}$, a volumetric number, N_V , of the order of $7 \times 10^{14} \text{m}^{-3}$ is obtained, which represents a volume fraction, f_V , of about 0.136. Assuming all Si particles are spherical, their average

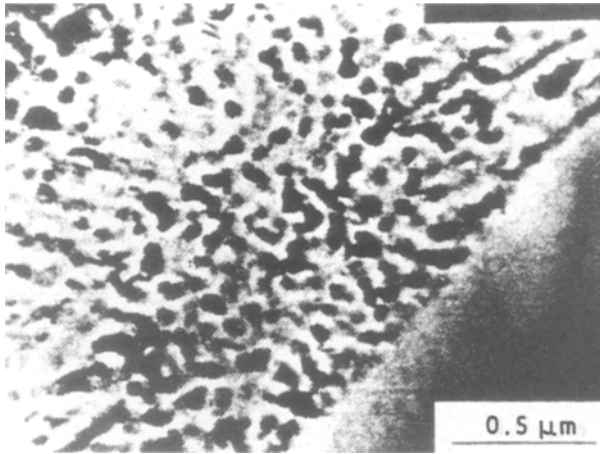


Figure 4 A bright-field micrograph corresponding to Al-Si-Sr loose powder.

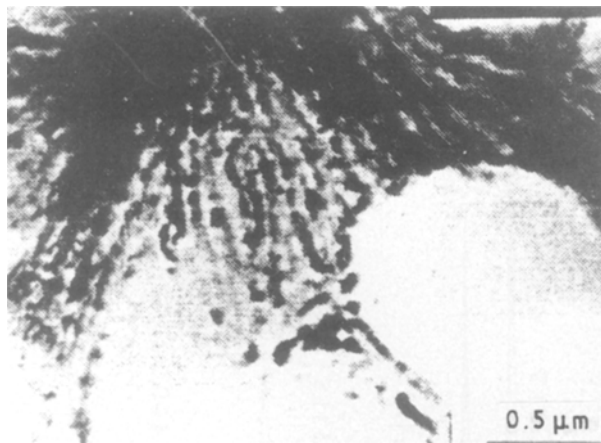


Figure 5 A bright-field micrograph of as-extruded Al-12% Si powder.

diameter can be calculated as follows:

$$d = \left(\frac{6f_v}{\pi N_v} \right)^{1/3} = 160 \text{ nm}$$

Specimens from extruded Al-12% Si were aged at 200, 300 and 400 °C for times up to 10 h. Optical examination did not reveal noticeable microstructural changes on ageing at 300 °C. After 3 h at 400 °C, crystals of silicon up to 2 μm could be measured. After 10 h at this temperature, the size of the Si particles was about 4 μm. At 500 °C, their respective diameters were 4 and 8 μm.

3.1.2. Al-Li-Si alloys

Four Al-Li-Si alloys were examined in the present work. The microstructures were examined by light microscopy. For ALS1 and ALS2 alloys, the essential microstructural feature was the presence of primary α-Al crystals separated by the eutectic product (Al + AlLiSi phases). Increasing the silicon content to 4% resulted in replacing the primary α-Al crystals with primary AlLiSi crystals surrounded by silicon-depleted regions. The rest of the matrix decomposed into the eutectic mixture, constituting about 80% of

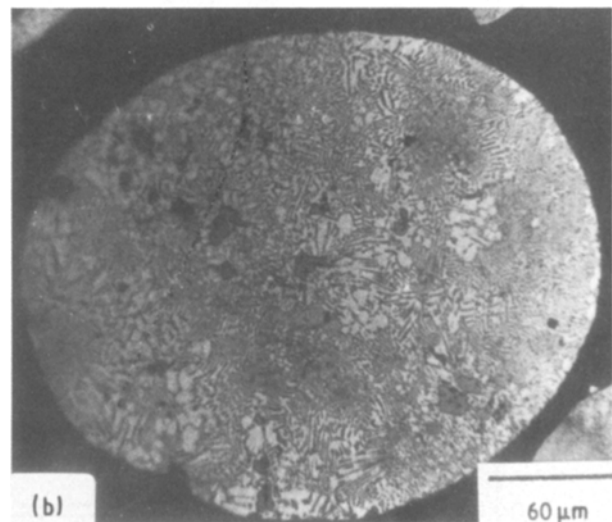
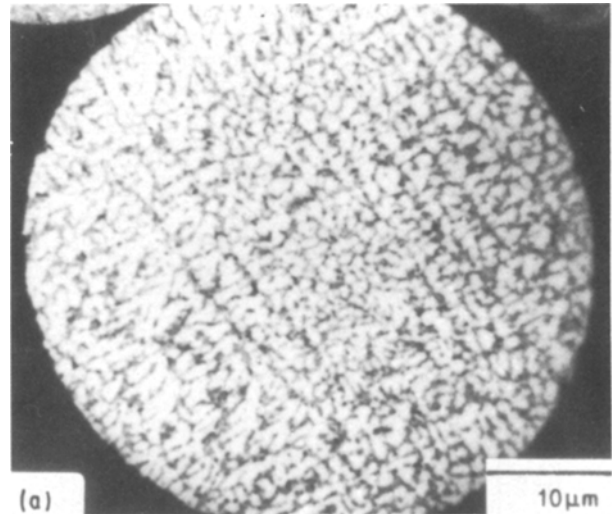


Figure 6 Optical micrographs of ALS4 powder of different particle sizes: (a) ~ 50 μm, (b) ~ 200 μm.

the microstructure. Thus, the ternary eutectic composition for Al-2.5% Li-Si system occurs at Si > 4 wt %, instead of 12.6 wt % for binary Al-Si alloys.

The microstructure of the powder particles is greatly influenced by the powder particle size. Considering ALS4 alloys, for sizes up to 50 μm the microstructure (Fig 6a) reveals a dendritic structure with AlLiSi fine precipitates delineating the secondary dendrite arms (cooling rate 10⁶ °C s⁻¹). Fig. 6b is the microstructure for a powder particle size of the order of 200 μm (cooling rate ~ 10⁴ °C s⁻¹). The main feature is the formation of primary crystals of AlLiSi phase.

According to the Al-Li equilibrium diagram [5], the maximum solubility of Li in α-Al is 5 at %. The present alloy contains ~ 10 at %, whereas the formation of the AlLiSi phase needs 4 at % Li. Therefore, this alloy does not show an effective volume fraction of δ'-Al₃Li precipitates which are responsible for strengthening the alloy on ageing.

The effect of rapid solidification appears in reducing both the amount and size of AlLiSi primary crystals. Comparing Fig. 6a and b emphasizes the extended solid solubility, enhanced by increasing the cooling rate via decreasing the powder particle size.

The above-mentioned results allow us to conclude that if the Si/Li atomic concentration ratio is less than unity, all the silicon is included in the AlLiSi phase. If the Li concentration is less than 5 at %, Li remains in solid solution with no occurrence of δ' -Al₃Li precipitation. Thus, for obtaining an appreciable volume fraction of Al₃Li precipitates in the presence of Si, the concentration of Li in the alloy should be sufficiently high. This, in turn, further reduces the alloy density. According to our density measurements, performed on loose powders containing various concentrations of Si and Li, the density of an Al–Li–Si alloy can be expressed by the relation

$$\rho = 2.7 - 0.24C_{Si} - 2.008C_{Li}$$

where C_{Si} and C_{Li} are, respectively, the atomic concentrations of Si and Li. The expected density of the present alloy is $2.4 \times 10^3 \text{ kg m}^{-3}$.

During ageing of the hot-extruded alloy at 200 °C for 100 h, precipitates of Al₃Li phase appeared inside the α -Al grains; they were $\sim 30 \text{ nm}$ in diameter. Some precipitate-free zones appeared around the initial AlLiSi phase particles (Fig. 7a). The size of the latter remained constant but new, very fine particles of AlLiSi phase precipitated inside the α -Al grains; they were 15 nm in diameter and led to the formation of a narrow precipitate-free zone along the grain boundaries.

In the ALS2 alloy, the precipitation of Al₃Li was again visible but the density of these precipitates was

lower (Fig. 7b and c). The initial AlLiSi precipitates remained practically unchanged and very fine new ones appeared with greater density. In the ALS4 and ALS8 alloys no more Al₃Li phase precipitated and only a very small enlargement of the previous AlLiSi precipitates was the main observation (Fig. 7d).

3.1.3. The Al–Li–Fe system

Observations made by SEM on the outer surfaces of the particles of AL3 loose powders revealed a well-defined dendritic structure as shown in Fig. 8a. Fig. 8b is a typical microstructure of AL3F2 powders. The absence of a growth direction makes us believe that the microstructure is mainly comprising cells or grains. The sides of these grains are not always straight.

Fig. 9a is an electron micrograph obtained from AL3 powders showing a dendrite-like structure with an arm spacing $\sim 0.3 \mu\text{m}$ in colonies of 2 to 3 μm diameter. Selected-area diffraction patterns and dark-field microscopy identified the dendritic-like phase as α -Al solid solution with a common orientation throughout each colony. The interdendritic network phase could be indexed on the basis of δ' -Al₃Li phase.

The TEM micrograph in Fig. 9b is produced from the powder particles of AL3F2 alloys. Near the centre of each grain, a coarse particle of AlFe (as could be identified from analysing the corresponding electron diffraction pattern) can be seen. The nucleation and

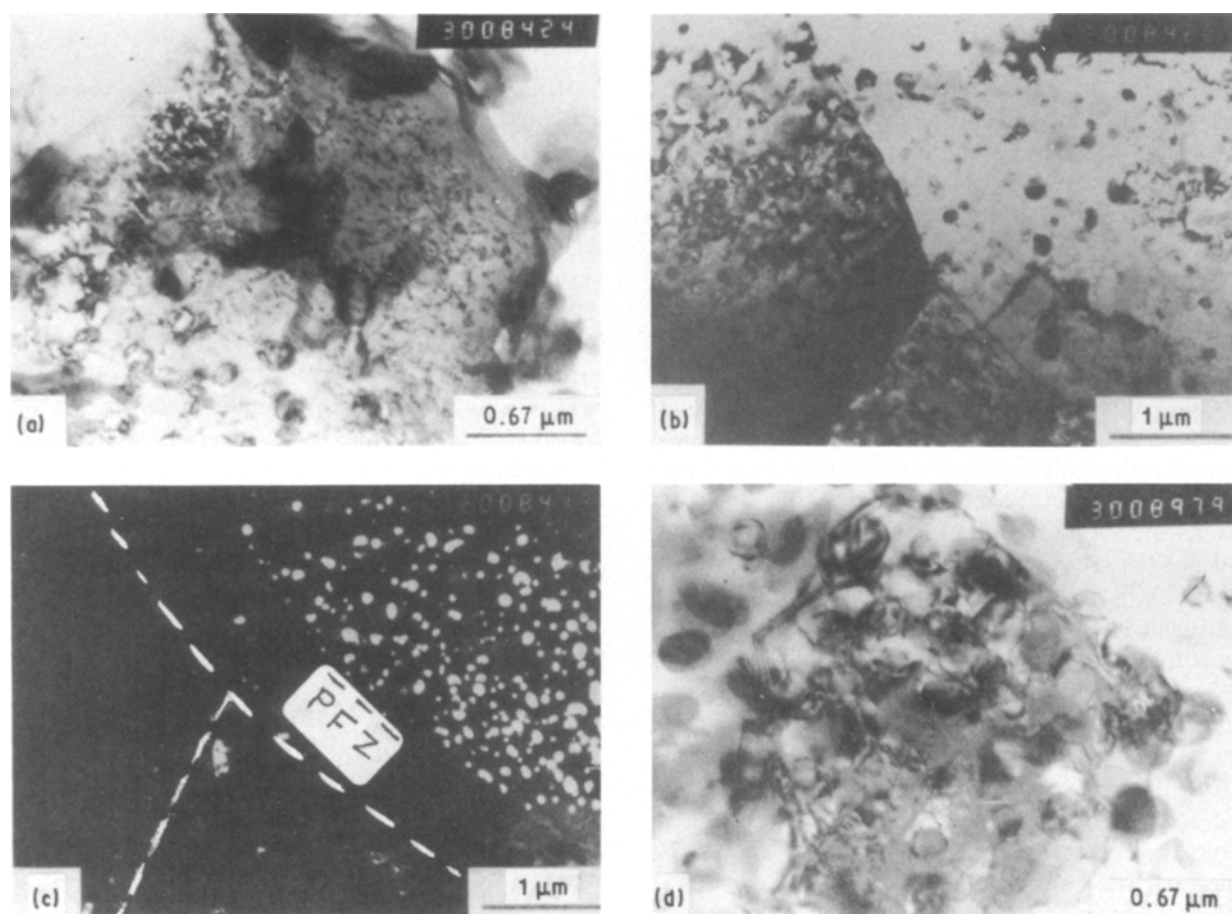


Figure 7 TEM micrographs of Al–Li–Si extruded powders, aged at 200 °C for (a) ALS1, bright field; (b) ALS2, bright field; (c) ALS2 δ' , dark field; (d) ALS4, bright field.

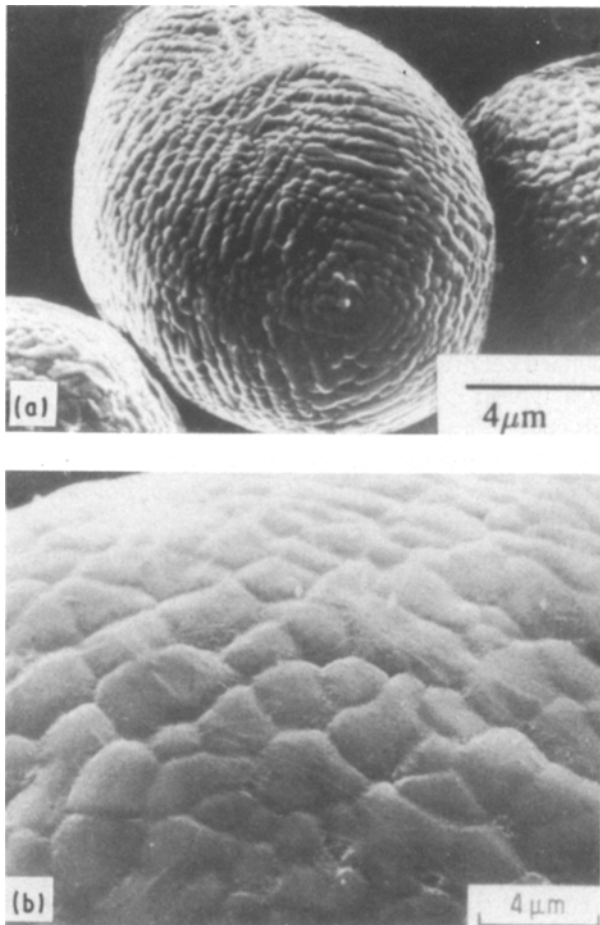


Figure 8 SEM micrographs of outer surfaces of loose powders: (a) AL3, (b) AL3F2.

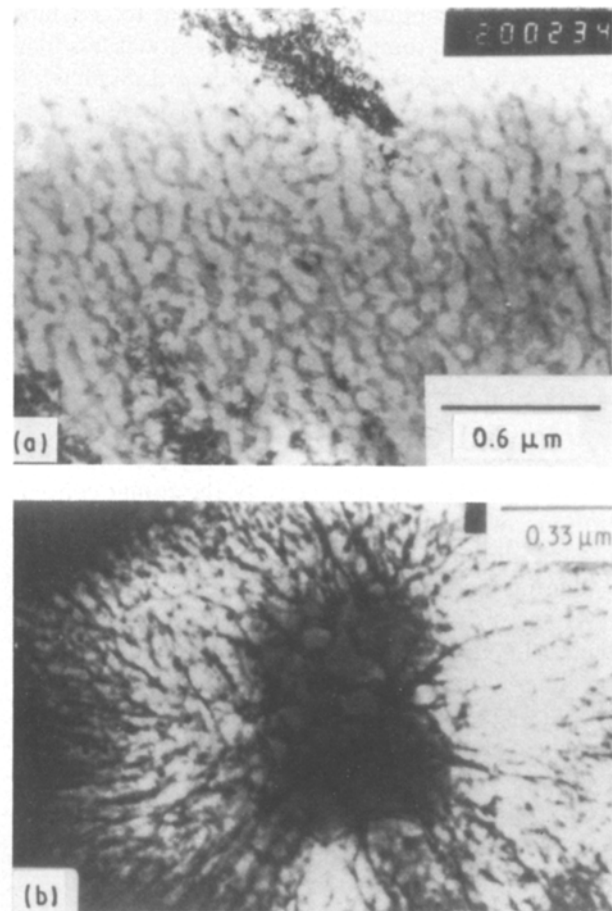


Figure 9 TEM micrographs produced from loose powders: (a) AL3, (b) AL3F2.

growth of primary AlFe is followed by the subsequent nucleation and growth of primary aluminium dendrite arms. The primary aluminium is found to grow radially outward from the central intermetallic particles. The secondary dendrite arms are delineated by the precipitation of both Al₃Fe particles.

Jones [12] has reported a similar observation in a rapidly solidified Al–11 wt % Fe hypereutectic alloy made by melt-spinning. He refers to this microstructure as zone B, and it is characterized by large intermetallics surrounding primary aluminium dendrites. It should be noted that the intermetallics appear to be located at the centres of local solidification fronts. This would suggest that the intermetallic was the first solid to nucleate and grow, followed by primary aluminium and not the reverse.

Fig. 10a is a TEM micrograph obtained from AL3 as-extruded powder (transverse section). The microstructure is comprised of fine equiaxed grains (2–5 μm). Coarse precipitates due to δ-AlLi phase at the grain boundaries as well as within the grains are viewed. Fig. 10b represents the microstructure of as-extruded AL3F2 powder. The microstructure is microcrystalline with grain sizes in the range 1 to 3 μm. Dense precipitation due to Al₃Fe and Al₆Fe phase particles is marked.

The TEM micrograph shown in Fig. 11a corresponds to AL3 alloy after solid-solution treatment. The microstructure is characterized by the absence of

δ-AlLi phase particle precipitates. The grain size varied between 2 and 5 μm. Homogeneous precipitation of δ'-Al₃Li phase particles with diameters up to 4 nm was first observed immediately after quenching and refrigerating in liquid nitrogen (Fig. 11b). The presence of these precipitates was not affected by the grain boundary.

When an alloy containing sufficient Li is quenched from the α-single phase field, decomposition of the supersaturated solid solution takes place by homogeneous precipitation of the ordered δ' phase. Nozato and Nakai [13] have deduced from thermal analysis that δ' formation cannot be suppressed by ice-water quenching in alloys containing more than 1.7% Li. The δ'-Al₃Li phase has an LI2 type superlattice structure and a spherical shape possessing cube-cube orientation with respect to the matrix.

Fig. 12 is produced from AL3F2 alloy after solution heat-treatment. Two types of precipitates could be identified:

- (a) coarse spherical particles (> 100 nm) due to Al₆Fe phase (open triangle) placed at the grain boundaries as well as at their interiors; and
- (b) needle-like particles due to Al₃Fe phase (closed triangle) distributed mainly intragranularly.

The solution heat-treated materials were aged artificially at 200 °C (under a helium atmosphere) for different ageing times. The presence of Fe did not seem to

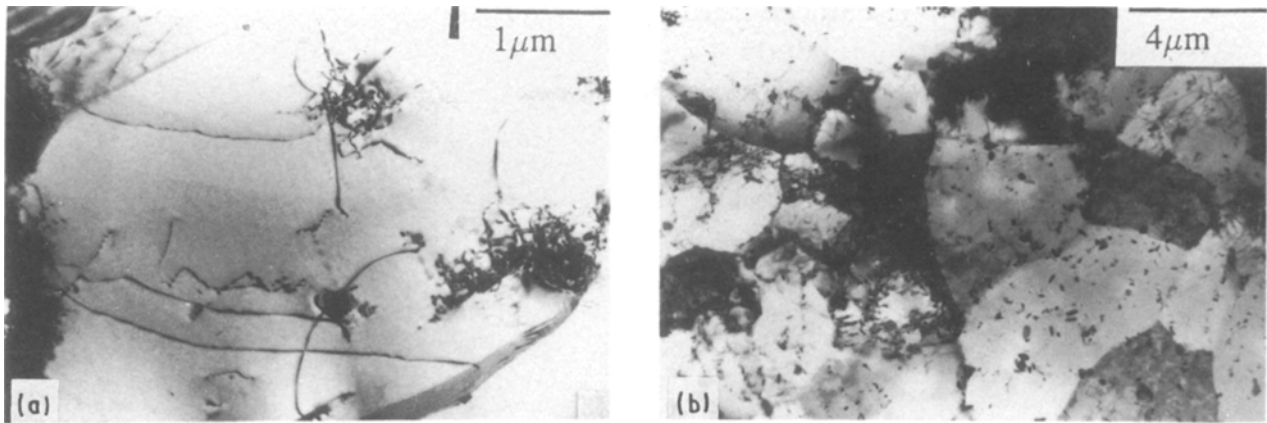


Figure 10 TEM micrographs obtained from hot-extruded alloys: (a) AL3, (b) AL3F2.

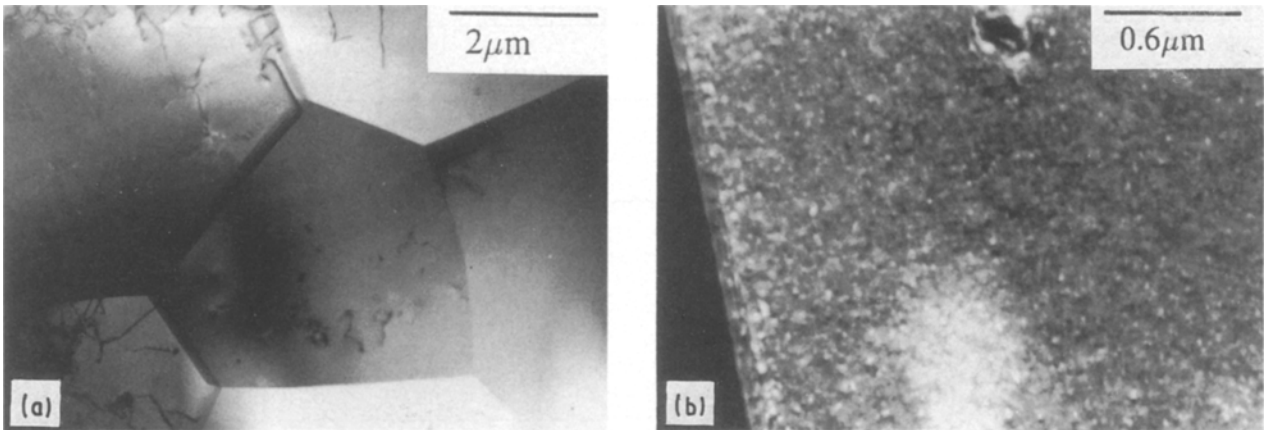


Figure 11 TEM micrographs obtained from solution heat-treated AL3 alloy: (a) bright field, (b) δ' dark field.

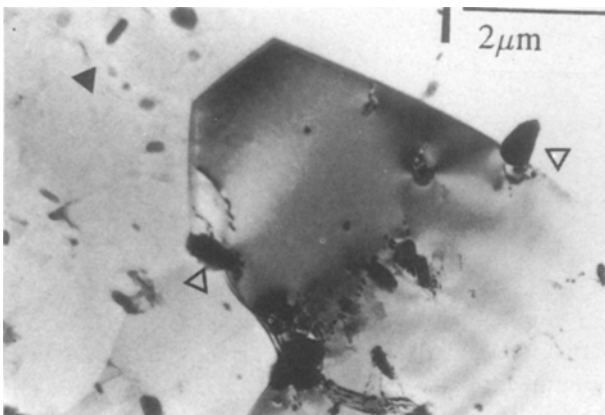


Figure 12 TEM micrograph of solution heat-treated AL3F2 alloy.

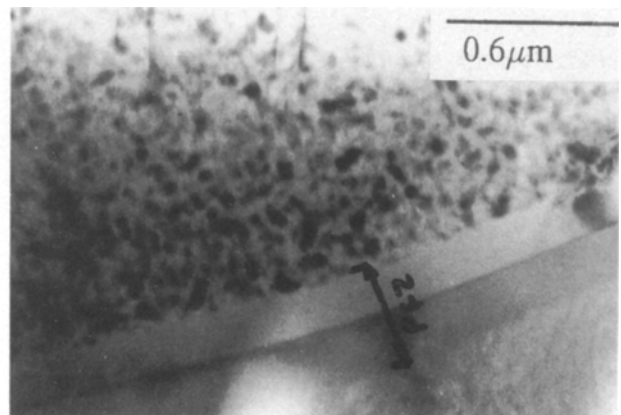


Figure 13 TEM micrograph of AL3 alloy, aged at 200 °C for 16 h.

have any significant effect on the kinetics of either the precipitation-free zone (PFZ) formation or δ' -Al₃Li phase particle coarsening.

Fig. 13 shows the occurrence of a wide PFZ (280 nm) in the vicinity of the grain boundary when the AL3 alloy was aged at 200 °C for 16 h. The average δ' particle diameter is about 40 nm. Fig. 14a and b are bright- and dark-field micrographs obtained from the AL3F2 alloy treated similarly. These figures emphasize the role of rapid solidification in increasing the extent of solid solubility. An important fraction of iron was in solid solution after ice-water quenching and it

decomposed uniformly throughout the grain after ageing. This process is expected to enhance strengthening of the soft PFZs observed in AL3 alloy (Fig. 13).

3.2. Mechanical properties

3.2.1. Al-Si alloys

The tensile properties of as-extruded Al-Si powders compared to ingot metallurgy (IM) are summarized in Table III. The properties of binary Al-12% Si alloy are markedly improved by rapid solidification: $\sigma_{0.2}$ by 100%, σ_E by 60%, EL by 100% and RA by > 400%.

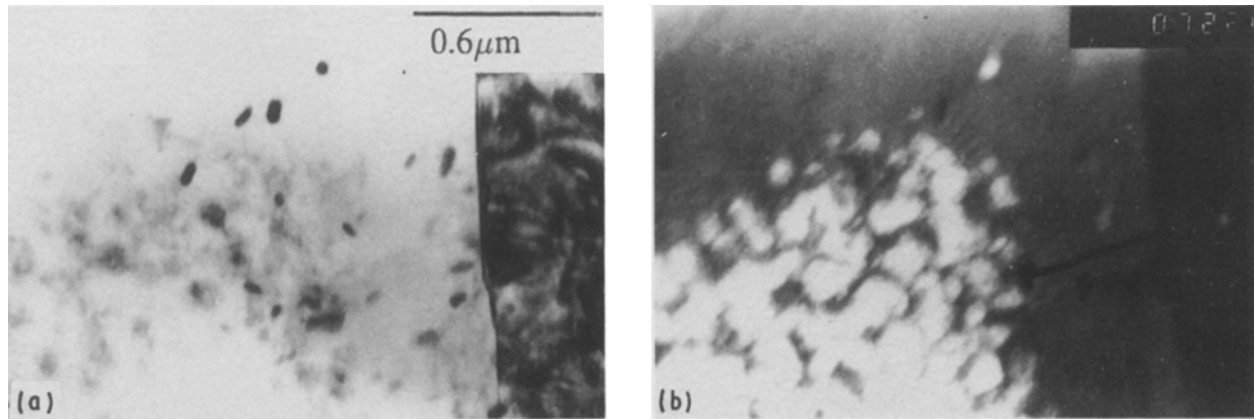


Figure 14 TEM micrographs of AL3F2 alloy aged at 200 °C for 16 h: (a) bright field, (b) δ' dark field.

TABLE III Mechanical properties of as-extruded powder ($\sigma_E = F_{max}/S_0$, $\sigma_R = F_{max}/S_r$, $El = \Delta L_0$ and $RA = \Delta A/A_0$)

Alloy	$\sigma_{0.2}$ (MPa)	σ_E (MPa)	σ_R (MPa)	EL (%)	RA (%)
Al-12% Si	162	244	324	19	47
Al-Si-Sr	197	283	365	18	51
Al-Si (IM)	79	185	202	9	9

Table IV gives the tensile results obtained after ageing the extruded Al-12% Si powders at 200, 300, 400 and 500 °C. After 10 h at 200 and 300 °C, not much change could be observed in the elastic limit and ultimate tensile strength values, whereas the ductility increased from 19 to 24%. At 400 and 500 °C, a significant reduction in both $\sigma_{0.2}$ and σ_E was obtained, with an increase in alloy ductility that reached 31% at 500 °C.

3.2.2. Al-Li-Si alloys

Due to shortage of specimens, tensile tests could not be conducted successfully for these alloys.

3.2.3. Al-Li-Fe alloys

Tensile test specimens from both alloys were aged at 200 and 220 °C for 16 h, and 24 h at each temperature. In each case, four specimens were tested and the average values are listed in Table V. Typical load-displacement curves produced from AL3F2 alloy are presented in Fig. 15.

During the solution heat-treatment process (540 °C/30 min), all the δ -AlLi particles as well as a fraction of Al_3Fe and Al_6Fe particles were dissolved in the matrix. This process, also, was associated with the annealing of the internal stresses.

Age-hardening at 200 °C took place after an incubation period of about 14 h and reached its maximum after 20 h. Increasing the ageing temperature resulted in accelerating the time required to reach maximum strength.

As expected, the presence of Al_3Fe dispersoid particles leads to a noticeable improvement in both the strength and ductility of AL3F2 alloy as compared to AL3 material (see Table V). Considering an alloy containing in weight 96.2% Al, 2.5% Li and 1.3% Fe,

TABLE IV Mechanical properties of extruded Al-12% Si powders, aged at 200, 300, 400 and 500 °C for various times

Ageing temperature (°C)	Ageing time (h)	Property		
		$\sigma_{0.2}$ (MPa)	σ_E (MPa)	EL(%)
200	2	—	—	—
	4	—	—	—
	10	169	237	22
300	2	151	218	23
	4	153	219	24
	10	158	216	24
400	2	134	202	25
	4	128	193	26
	10	123	186	27
500	2	105	173	29
	4	74	158	30
	10	74	156	31

the corresponding atomic composition is 90.6% Al, 9.16% Li and 0.6% Fe. Assuming that all lithium will be in the form of δ' - Al_3Li (density 2.33 g cm^{-3}), and all iron will be in the form of Al_3Fe phase (density $\sim 3.45 \text{ g cm}^{-3}$), under these conditions, the volume fraction of δ' will be close to 36.5% and that of Al_3Fe will be about 3.65%, i.e. one-tenth. It was found that such a volume fraction of Al_3Fe is enough to balance the loss of strength of the PFZs due to migration of δ' particles towards the grain centre.

It is interesting to compare our results with those previously published for alloys containing the same elements, Fe, Co and Ni. These are tabulated in Table VI. It is seen that for Al-Li binary alloys, materials made by powder metallurgy (PM) possess somewhat higher strength parameters compared with those obtained from ingot, made by classical casting. The observed low ductility for PM alloys is explicable in terms of the remarkable difference in the strength level

TABLE V Tensile Properties of AL3 and AL3F2 extruded powders

Treatment	AL3			AL3F2		
	$\sigma_{0.2}$ (MPa)	σ_m (MPa)	EL (%)	$\sigma_{0.2}$ (MPa)	σ_m (MPa)	EL (%)
540 °C/30 min + wq (= A)	72	196	19	75	178	19
A + 200 °C/16 h	319	395	4.5	372	440	5.5
A + 200 °C/20 h	312	394	5	366	432	6.7
A + 200 °C/24 h	—	—	—	360	430	7.5
A + 220 °C/16 h	281	348	6.0	310	387	8.0
A + 220 °C/10 h	254	318	7.0	311	386	9.0
A + 220 °C/24 h	—	—	—	266	354	10.5

TABLE VI Tensile properties of some Al-Li-X alloys aged differently at 200 °C

Alloy composition	Symbol ^a	$\sigma_{0.2}$ (MPa)	σ_m (MPa)	EL (%)	Ref. ^b
Al-2.5Li	0	312	394	5	PW
	0	296	396	5.5	14
	*	256	385	8.0	15
	*	264	376	5.0	15
Al-1.9Li	*	177	213	2.0	16
Al-3Li	0	295	—	5.0	17
Al-2.7Li-1.3Fe	0	366	430	6.2	PW
Al-2.95Li-0.64Co	0	296	409	8.3	14
Al-3.8Li-0.48Fe-0.43 Co	0	391	468	4.5	14
Al-3.56Li-0.36Fe-0.48Ni	0	378	464	4.8	18

^a0: rapidly solidified alloys, *: classically solidified alloy.

^bPW: present work.

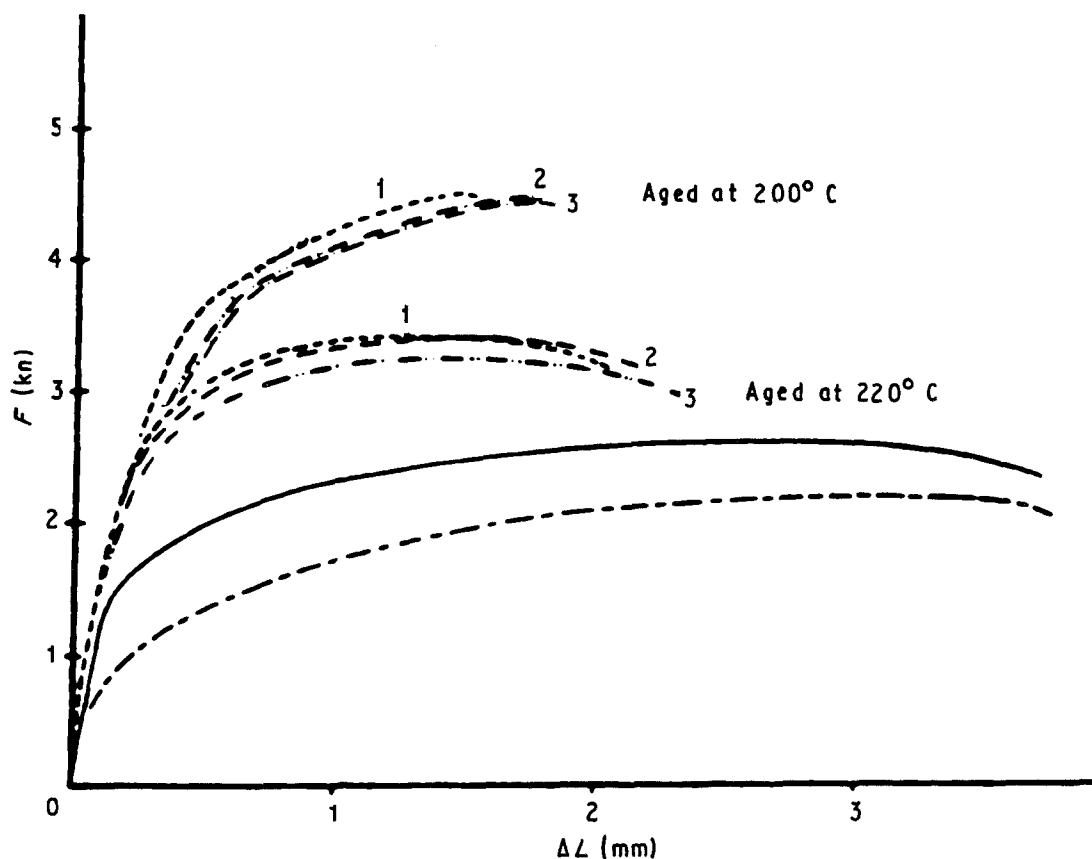


Figure 15 Typical load–displacement curves obtained from AL3F2 alloy subjected to different heat treatments: (—) as-extruded alloy, (---) after solution heat-treatment.

between the PFZs and the rest of the grain. It should be noted that for these alloys the volume fraction of the PFZs, when the material is aged at 200 °C, is approximately 24% for 16 h and 50% for 100 h ageing

time [19]. These PFZs lead to intergranular brittle fracture. Thus, the presence of Al₃Fe dispersoids greatly enhances transgranular ductile fracture through strengthening the PFZs [20].

4. Conclusions

4.1. Al–Si alloys

1. Solidification occurs by heterogeneous nucleation at the interface with the atmosphere (helium) followed by propagation of the solidification front towards the particle centre. In this case, we do not observe sufficient undercooling and thus obtain a “non-segregated” solid solution.

2. For binary Al–12% Si alloys, the tensile properties of hot-extruded powders are much improved compared to those obtained from alloys made by ingot metallurgy.

4.2. Al–Li–Si alloys

1. Addition of 3% Li to the Al–Si alloys shifts the eutectic point to less than 4 wt % Si. The eutectic structure is a mixture of aluminium and AlLiSi phases.

2. If the Si/Li ratio is less than unity, all the silicon is included in the AlLiSi particles. If the Li concentration is too low, it remains in solid solution with no δ' -Al₃Li precipitation.

3. For a given volume fraction of Al₃Li, addition of Si permits an increase in the concentration of Li in the alloy, which produces a remarkable decrease in the alloy density.

4.3. Al–Li–Fe alloys

1. For Al–2.5 wt % Li–1.3 wt % Fe, in addition to δ' -Al₃Li phase precipitates, Al₃Fe (needle-like) and Al₆Fe (globular) phase precipitates are present. The former phase appears mainly in the grain interiors whereas the latter phase occurs at the grain boundaries.

2. The volume fraction of Al₃Fe dispersoids is one-tenth that of the Al₃Li. The formation of this phase (Al₃Fe) is not affected by the presence of the grain boundaries, and is enough to strengthen the PFZs.

3. The presence of Fe and, hence, Al₃Fe particles leads relatively to a better combination of strength and ductility when compared with Al–Li binary alloys.

Acknowledgements

One of the authors (FHS) would like to acknowledge with gratitude the financial support received from the Natural Sciences and Engineering Research Council of Canada, the Fondation Sagamie de l'Université du Québec à Chicoutimi and the Société d'électrolyse et de chimie Alcan (SECAL).

References

1. M. J. AZIZ, *J. Appl. Phys.* **53** (1982) 2.
2. J. L. MURRAY, *Mater. Res. Soc. Symp. Proc.* **19** (1983) 251.
3. G. CHAMPIER and F. H. SAMUEL, in Proceedings of Conference on Aluminum–Lithium III, Oxford, UK, July 1985 (Institute of Metals, London, 1988) p. 131.
4. T. H. SANDERS Jr, E. A. LUDWICZAK and R. R. SAWTELL, *Mater. Sci. Engng*, **43** (1980) 247.
5. M. HANSON and K. ANDERKO, “Constitution of Binary Alloys” (McGraw-Hill, New York, 1958, and supplement 1985) p. 104.
6. R. G. BOURDEAU, US Patent 4 217 082 (1980).
7. J. A. KING, US Patents 4 025 249 (1977) and 4 053 764 (1977).
8. P. R. HOLIDAY and R. J. PATTERSON, US Patent 4 078 873 (1978).
9. P. COULOMB, “Les Textures dans les Métaux de Réseau Cubique”, (Dunod, Paris, 1972).
10. C. C. LEVI and R. MEHRABIAN, *Met. Trans. A* **13A** (1982) 13.
11. *Idem, ibid.* **13A** (1982) 221.
12. H. JONES, *Mater. Sci. Engng* **5** (1970) 1.
13. R. NOZATO and F. R. NAKAI, *Trans. JIM* **18** (1977) 679.
14. K. K. SANKARAN, S. M. L. SASTRY and J. E. O'NEAL, in Proceedings of Conference on Aluminum–Lithium I, Stone Mountain, May 1980 (TMS-AIME, 1981) p. 189.
15. T. H. SANDERS Jr, E. A. LUDWICZAK and R. R. SAWTELL, *Mater. Sci. Engng* **43** (1980) 247.
16. B. NOBEL, S. J. HARRIS and K. DINSDALE, *J. Mater. Sci.* **17** (1982) 461.
17. S. M. L. SASTRY and J. E. O'NEAL, in Proceedings of Conference on Aluminum–Lithium II, Monterey, April 1983, (TMS-AIME, 1984) p. 79.
18. I. G. POLMER, R. E. LEWIS and D. D. CROOKS, in Proceedings of Conference on Rapid Solidification Processing: Principles and Technologies II, Reston, May 1980 (Claitor 1980) p. 342.
19. F. H. SAMUEL, *J. Mater. Sci.* **21** (1986) 3097.
20. F. H. SAMUEL and G. CHAMPIER, *ibid.* **22** (1987) 3851.

Received 10 May

and accepted 19 July 1991